



Manganese doped-iron oxide nanoparticle clusters and their potential as agents for magnetic resonance imaging and hyperthermia.

Journal:	<i>Physical Chemistry Chemical Physics</i>
Manuscript ID	CP-ART-03-2016-002094.R1
Article Type:	Paper
Date Submitted by the Author:	27-May-2016
Complete List of Authors:	<p>Casula, Maria; Universita di Cagliari, Dipartimento di Scienze Chimiche Conca, Erika; Università di Cagliari, Dipartimento di Scienze Chimiche e Geologiche Bakaimi, Ioanna; Uniiversity of Southampton, Physics and Astronomy Ayyappan, S.; Istituto Italiano di Tecnologia, Nanochemistry Materia, Maria; Istituto Italiano di Tecnologia, Nanochemistry Casu, Alberto; King Abdullah University of Science and Technology (KAUST), Biological and Environmental Sciences and EGINEERING Division (BESE) falqui, andrea; King Abdullah University of Science and Technology, Sogne, Elisa; King Abdullah University of Science and Technology (KAUST), Biological and Environmental Sciences and EGINEERING Division (BESE) Pellegrino, Teresa; Istituto Italiano di Tecnologia Kanaras, Antonios; University of Southampton, Physics and Astronomy</p>



Journal Name

ARTICLE

Manganese doped-iron oxide nanoparticle clusters and their potential as agents for magnetic resonance imaging and hyperthermia

¹Received 00th January 20xx,
Accepted 00th January 20xx

DOI: 10.1039/x0xx00000x

www.rsc.org/

Maria F. Casula,^{a,b} Erika Conca,^{a,b} Ioanna Bakaimi,^c Ayyappan Sathya,^d Maria Elena Matera,^d Alberto Casu,^e Andrea Falqui,^e Elisa Sogno,^e Teresa Pellegrino,^d and Antonios G. Kanaras^{c,*}

A simple, one pot method to synthesize water-dispersible Mn doped iron oxide colloidal clusters constructed of nanoparticles arranged into secondary flower-like structures was developed. This method allows the successful incorporation and homogeneous distribution of Mn within the nanoparticle iron oxide clusters. The formed clusters retain the desired morphological and structural features observed for pure iron oxide clusters, but possess intrinsic magnetic properties that arise from Mn doping. They show distinct performance as imaging contrast agents and excellent characteristics as heating mediators in magnetic fluid hyperthermia. It is expected that the outcomes of this study will open up new avenues for the exploitation of doped magnetic nanoparticle assemblies in biomedicine.

Introduction

The exploitation of colloidal inorganic nanoparticles in biomedical applications is of great research interest.^{2, 3} Nanoparticles offer a range of advantages deriving from their ligand coating as well as the properties of the inorganic core.⁴ For example, the choice and density of ligands on the nanoparticle surface determines colloidal stability, targeted ability and reactivity of the nanoparticles.⁵⁻⁹ Additionally, the chemical composition of the inorganic core defines the optical, thermal, mechanical or magnetic properties of the nanoparticles, which are directly relevant for imaging and therapeutic biomedical applications.¹⁰⁻¹³ Among various types of inorganic nanoparticles, magnetic nanoparticles have attracted particular interest because of their tunable thermal properties useful for therapeutic purposes as well as their intrinsic performance as contrast agents in magnetic resonance imaging (MRI).¹⁴⁻¹⁹ Indeed, the excellent *in vivo* contrast of some types of magnetic nanoparticles (e.g. super-

paramagnetic iron oxide nanoparticles) led them to incorporation in commercial MRI formulations approved both by the U.S. and E.U. drug screening agencies.²⁰ However, in many cases the performance of magnetic nanoparticles may deteriorate from a combination of factors including lack of robustness in complex environments and loss of structure.

In the quest for improved nanoparticulate systems with enhanced magnetic properties, in 2007 the Yin group developed a chemical method to create assemblies of superparamagnetic iron oxide nanoparticles coated and held together by a low molecular weight polymer (i.e. polyacrylic acid (PAA)).²¹ The sizes of these nanoparticle assemblies, namely colloidal nanoparticle clusters (CNCs), are tunable from 20-200 nm following adjustment of several reaction parameters (e.g. reaction temperature and water content). In comparison to individual nanocrystals, CNCs possess novel and enhanced optomagnetic features, such as photonic crystal behavior, as well as decreased surface disorder in comparison to individual nanoparticles. Moreover, the large size of the small nanoparticle assemblies increases the saturation magnetisation of the cluster, which retains the superparamagnetic characteristics of the individual small nanoparticles. For these reasons CNCs are strong candidates for a range of applications in photonics, catalysis and lately biomedicine.

Recently, Gazeau and co-workers showed that exchange coupling in iron oxide CNCs changes the dynamics of the magnetic moment in a way that both the longitudinal and transverse NMR relaxivities of the clusters are enhanced. Also they pointed out the remarkable heating efficiency of the clusters under an alternating magnetic field.^{22, 23} Further studies by Lappas and co-workers discussed extensively the

^a Department of Chemical and Geological Sciences and INSTM, University of Cagliari, 09042 Monserrato, Italy.

^b These authors contributed equally in this work.

^c Institute for Life Sciences, Physics and Astronomy, Faculty of Physical Sciences and Engineering, University of Southampton, Southampton, SO17 1BJ, U.K.

^d Istituto Italiano di Tecnologia, via Morego 30, 16145 Genoa, Italy.

^e Biological and Environmental Science and Engineering Division, KAUST, Jeddah, Saudi Arabia

† Footnotes relating to the title and/or authors should appear here.

Electronic Supplementary Information (ESI) available: Histogram of cluster size distribution as obtained by TEM analysis, DLS analysis, comparison of XRD patterns for pure Fe₃O₄ and MnFe₂O₄, ICP analysis, additional hyperthermia and relaxometric characterization of the Mn-doped clusters. See DOI: 10.1039/x0xx00000x

correlation between the magnetic and structural characteristics of CNCs.²⁴⁻²⁶ Both groups concluded that CNCs hold superior tunable magnetic properties, which are of strong potential for applications as MRI contrast agents and heating mediators in magnetic hyperthermia.^{23, 24} Furthermore, a recent study on the heating performance of iron oxide clusters in the size range of 45-98 nm pointed out that the optimal performance is obtained for cluster sizes of about 50 nm.²⁷

In this paper we present an alternative method to enhance the magnetic properties of CNCs by elemental doping of the superparamagnetic nanoparticles during the formation of the clusters. The elemental doping of CNCs holds significant potential for achieving the formation of high performance magnetic agents. Although the doping of the clusters can occur during an easy step of one-pot, rapid chemical synthesis, only few cases of relevant preliminary chemical studies have been reported so far.^{28, 29} In our experiments, Mn-doped iron oxide CNCs have been prepared and evaluated as MRI contrast agents as well as heating probes in magnetic fluid hyperthermia. These nanomaterials may hold a great potential for biomedical applications and highlight the need of more synthetic efforts to enrich the library of functional doped-CNCs.

Results and discussion

Synthesis of Mn-doped iron oxide CNCs

The general chemical route for the synthesis of the magnetic clusters involves the chemical decomposition of a mixture of iron (III) chloride and manganese (II) chloride salts at elevated temperature. Manganese was chosen as a typical dopant for iron oxide nanoparticles, mainly because of its suitability (in terms of charge and size) to replace iron (II) cations in the crystal structure of the nanoparticles. Diethylene glycol (DEG), a solvent with a high boiling point (245°C) was used as the polar medium to dissolve the precursors, while polyacrylic acid was employed as a non-toxic surfactant, which easily complexes with manganese and iron metals. An injection of a hot solution of sodium hydroxide in DEG initiates the nucleation of the precursors, which form Mn-doped iron oxide nanoparticles. These nanoparticles immediately aggregate into three dimensional flower-like shape structures, wrapped with the excess of polyacrylic acid molecules present in the vicinity. The large number of carboxylic groups on the surfactant either binds to the nanoparticle surface or extends to the outer part of the clusters, which equips them with high stability in polar solvents.

Characterization of Mn-doped iron oxide CNCs

The morphology of the synthesized materials was characterized by transmission electron microscopy (TEM), as shown in **Figure 1**. TEM revealed that the magnetic clusters were relatively monodispersed with an assembled arrangement. A statistical analysis on TEM images showed that the average cluster size was 50 ± 15 nm (see **Figure S1**). Further characterization by High Resolution TEM (HRTEM) indicated that the morphology of the Mn-doped iron oxide

CNCs is similar to the secondary structure reported for pure iron oxide CNCs.²⁰ As shown in **Figure 1B**, individual spherical

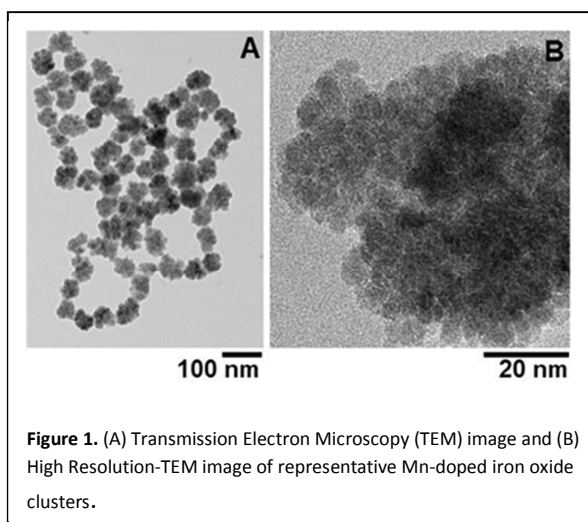


Figure 1. (A) Transmission Electron Microscopy (TEM) image and (B) High Resolution-TEM image of representative Mn-doped iron oxide clusters.

nanocrystals are aggregated together to form the larger cluster. The colloidal dispersity of the Mn-doped iron oxide clusters in water was evaluated by dynamic light scattering (DLS) (see supporting information **Figure S2**). The average hydrodynamic diameter was 54 ± 19 nm in good agreement with the inorganic cluster size as observed on TEM. In our experiments, the obtained manganese-doped iron oxide clusters remained stable in solution for months with no leakage of manganese or any other form of decomposition as evident from ICP and TEM (see also supporting information-Table S1). To detect the presence of iron and manganese in the clusters we used High Angle Angular Dark Field Scanning Transmission Electron Microscopy (HAADF-STEM).

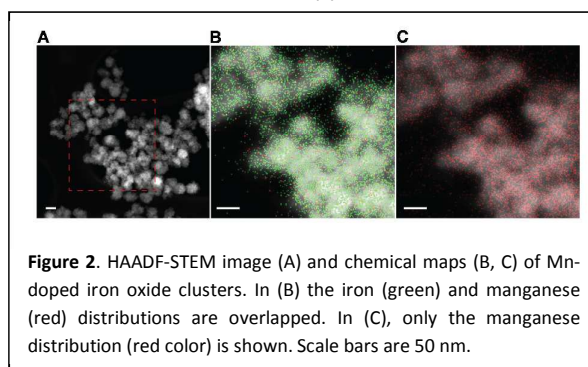


Figure 2. HAADF-STEM image (A) and chemical maps (B, C) of Mn-doped iron oxide clusters. In (B) the iron (green) and manganese (red) distributions are overlapped. In (C), only the manganese distribution (red color) is shown. Scale bars are 50 nm.

Figure 2 shows the STEM image of representative clusters and the distribution of iron (green) and manganese (red) within the clusters. From the images it is clear that Mn is well dispersed across the iron oxide clusters, without evidence of any kind of segregation. To determine the amount of Mn, which was incorporated in the clusters we used two techniques, the Energy Dispersive X-ray Spectroscopy (EDS) and Inductively Coupled Plasma Optical Emission Spectroscopy (ICP-OES). The EDS spectra, collected from several tens of clusters, showed a metal content of 88 mol% of Fe and 12 mol% of Mn (See Supporting Information, **Table S1**). This composition was at a

relevant agreement with the theoretical values based on the amount of initially added metals (85 mol% of iron and 15 mol% of manganese, respectively). Chemical analysis of the samples with ICP-OES gave very similar results to EDS, as the relative metal content was found to be 89 mol% of Fe and 11 mol% of Mn (See Supporting Information table S1). These measurements allowed us to safely conclude that the relative molar ratio of Fe: Mn in the clusters was about 7.5%.

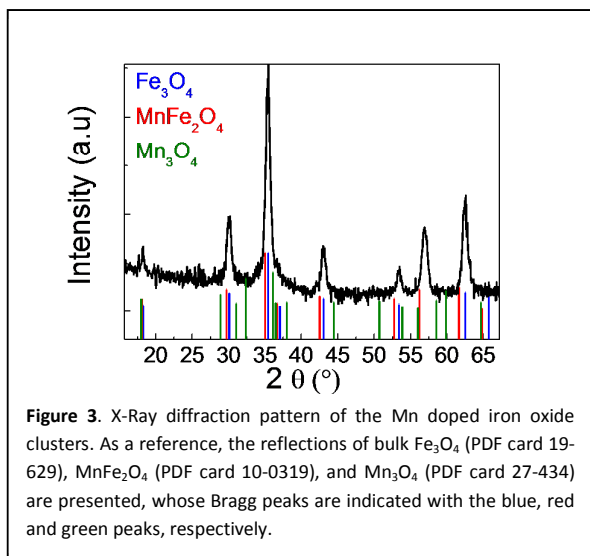


Figure 3. X-Ray diffraction pattern of the Mn doped iron oxide clusters. As a reference, the reflections of bulk Fe_3O_4 (PDF card 19-629), MnFe_2O_4 (PDF card 10-0319), and Mn_3O_4 (PDF card 27-434) are presented, whose Bragg peaks are indicated with the blue, red and green peaks, respectively.

Figure 3, shows the X-Ray Diffraction (XRD) analysis for the Mn-doped iron oxide clusters. Although the XRD pattern does not provide concrete evidence of Mn doping of the ferrite nanocrystals due to, both, a) the very low amount of Mn and b) the nearby cell parameters of isostructural Fe_3O_4 and MnFe_2O_4 (see also Supporting Information, **Figure S3**), our data clearly indicate that only a phase, which shows the typical crystalline pattern for a ferrite cubic spinel structure is present. No evidence of additional pure manganese oxide phases is observed as shown by comparison with the expected diffraction peaks for Mn_3O_4 , which features a spinel-type structure with a tetragonal distortion. The broadening of the experimental peaks suggests the occurrence of nanocrystalline domains within the Mn-doped iron oxide clusters. A line profile analysis, using the Scherrer equation corrected for instrumental broadening, indicates an average crystal domain size of 14 nm, in a relevant agreement with the model proposed by Yin and co-workers for the undoped iron oxide clusters.³⁰

The morphological characterization of the clusters by XRD and HRTEM reflects the flower-like structure of clusters, which, as it was mentioned earlier, is constituted by an ensemble of smaller individual nanocrystals acting as building blocks for the CNCs. It is important to point out that the individual nanocrystals don't share a common structural orientation and retain some features of independent single nanoparticles. This evidence is further supported by HRTEM analysis showing the orientation of the atomic planes among the individual nanoparticles (**Figure 4**). A similar orientation extended beyond the individual nanocrystals can be observed from

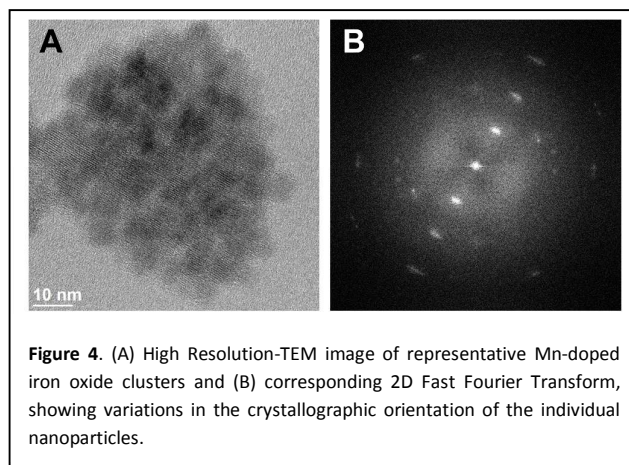


Figure 4. (A) High Resolution-TEM image of representative Mn-doped iron oxide clusters and (B) corresponding 2D Fast Fourier Transform, showing variations in the crystallographic orientation of the individual nanoparticles.

HRTEM images, but the presence of streaks instead of diffraction spots in the corresponding 2D Fast Fourier Transform makes it clear that the orientation among nanocrystals within the CNCs is not ideal and cannot be properly intended as a shared crystallographic orientation. These small variations hinder the crystallinity of the CNCs and suggest their intermediate nature between tightly, random-packed aggregates and well-ordered ones, aggregated in a sort of flower-like superstructures.

Magnetic structure of the Mn-doped iron oxide clusters

The introduction of Mn in the iron oxide clusters induces significant variations in the magnetic features of the clusters, which are directly correlated with the performance of the clusters at MRI and magnetic hyperthermia. While increasing the Mn content of the nanoparticles causes a higher saturation magnetisation,³¹ the effects of varying the Mn doping in colloidal CNCs are less straightforward. From a structural point of view, the introduction of Mn determines a decrease in size of both the nanoclusters and the primary nanocrystals, which is reflected in the variations observed in saturation magnetisation: for lower doping regimes ($0 < x < 0.5$) the net magnetisation is increased due to the Mn contribution, while for higher doping regimes ($x \geq 0.5$) the effects of size reduction prevail and cause its overall decrease.^{28, 32} Thus, our choice of introducing a low Mn doping content is intended as a conservative approach to boost the net magnetisation without heavily affecting the size of the nanocrystals and nanoclusters. In order to assess the effect of Mn-doping on our clusters, the DC magnetic susceptibility was measured as a function of temperature at low fields according to the ZFC-FC (Zero-Field Cooled-Field Cooled) protocols, while isothermal hysteresis loops were recorded at 5 K and body temperature (310 K).

Figure 5a shows that the ZFC-FC magnetisation curves do not show superparamagnetic relaxation of the clusters within the experimental temperature range. The maximum of the ZFC curve, defined as blocking temperature T_B , lies down well above room temperature ($T_B = 372$ K) and no actual superposition between the ZFC and FC magnetisation curves,

ARTICLE

Journal Name

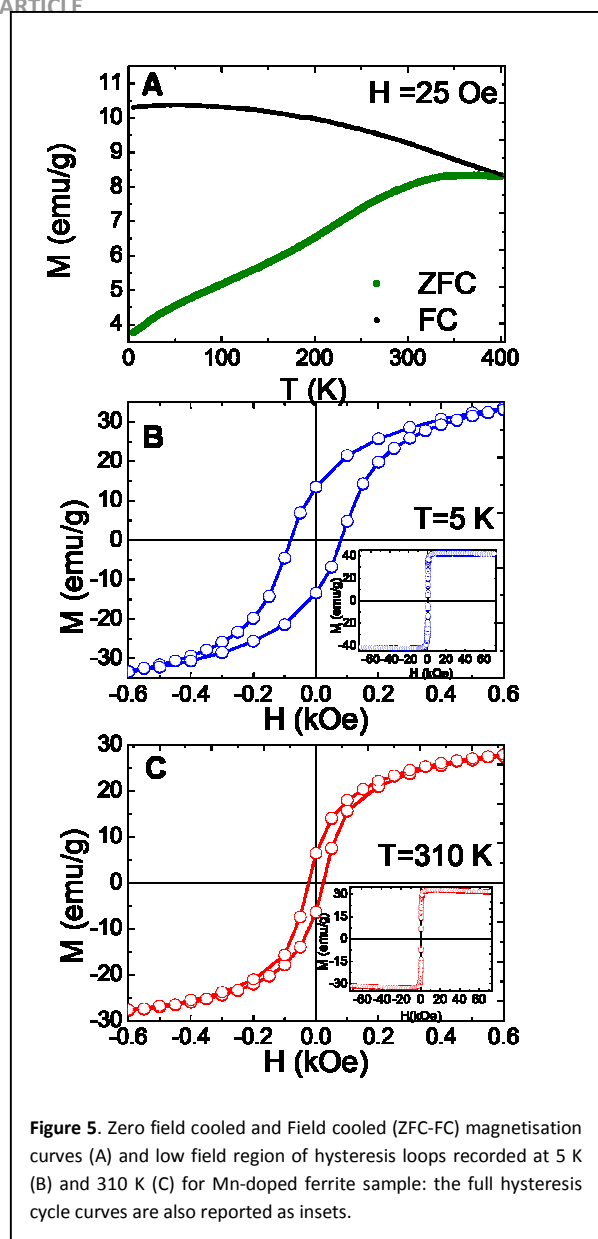


Figure 5. Zero field cooled and Field cooled (ZFC-FC) magnetisation curves (A) and low field region of hysteresis loops recorded at 5 K (B) and 310 K (C) for Mn-doped ferrite sample: the full hysteresis cycle curves are also reported as insets.

can be observed. This indicates a partially blocked state even at 400 K. When comparing the ZFC-FC curves of the Mn-doped iron oxide clusters with those of individual nanoparticles with Mn content and particle size comparable to that of our individual nanoparticles in the cluster,³³ a shift towards higher temperature can be clearly observed for our Mn-doped iron oxide clusters ZFC-FC curves. The broadening and shifting of the ZFC peak to higher temperature and the slow variation and the plateau in the low temperatures region of the FC magnetization curve both indicate moderate dipolar interactions.²⁵ In addition, as compared to tightly-packed clusters of interacting nanoparticles where a broad plateau has been reported,³⁴ the observed features are shallower. This relatively mild dipolar interaction effect within our CNCs can be attributed to the combined hindering caused by the presence of a superficial organic layer coating in the magnetic clusters and by the moderately ordered aggregates of

individual nanocrystals in the CNCs which is evidenced by HRTEM analysis.^{24, 35}

The hysteresis loops recorded at 5K and 310K (Figure 5B and 5C) provide further information on the magnetic

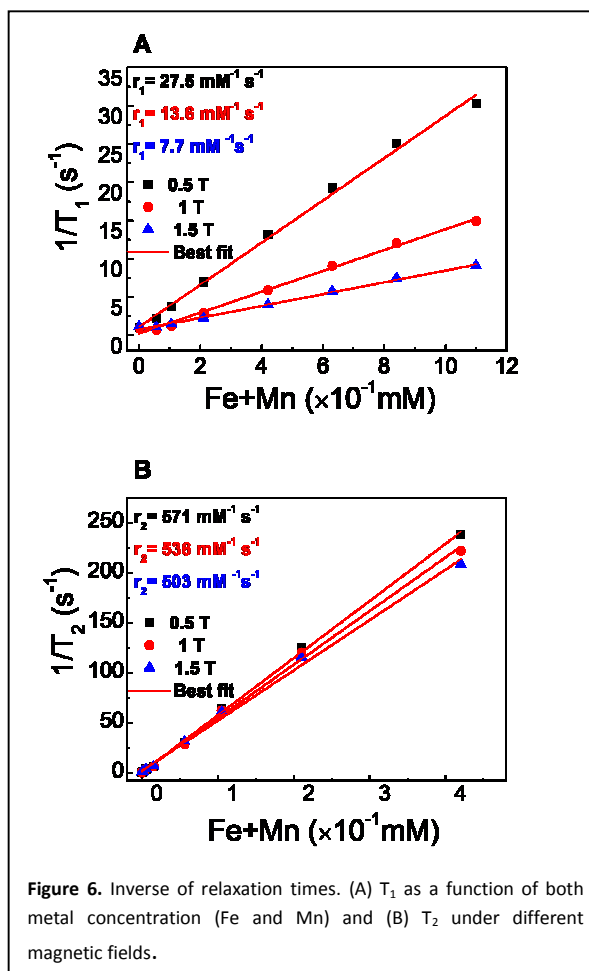


Figure 6. Inverse of relaxation times. (A) T_1 as a function of both metal concentration (Fe and Mn) and (B) T_2 under different magnetic fields.

characteristics of the clusters. The parameters obtained from the analysis of the curves recorded at both temperatures (see supporting information Table S1) are consistent with the presence of a soft magnetic system between interacting objects. Since the ZFC-FC curves did not show any superparamagnetic relaxation of the clusters up to 400 K, we conclude that the coercivity is not null because the clusters are still in a partially blocked state at 310 K. This observation differentiates our clusters from analogue systems, where superparamagnetic relaxation was achieved already at room temperature.^{28, 32} Additionally³⁶, the coercivity at 5 K and the saturation magnetisation recorded at 5 K and 310 K are lower than the ones registered for individual nanoparticles of Fe₃O₄, Mn_xFe_{3-x}O₄ and for similar types of clusters.^{28, 35, 37} The tight packing of the primary nanocrystals in the CNCs is obviously higher than what observed for systems constituted by individual, separate nanoparticles, thus the low coercivity values should be attributed to the presence of nanoparticle dipolar interactions already observed in the ZFC-FC curves, but

the saturation magnetization values require additional explanations.

While the presence of dipolar interactions may be either favourable or detrimental to the magnetic behaviour of clusters, they result in an overall decrease of the magnetic features of clusters composed by immobilized nanoparticles^{1, 38}, possibly due to the hindrance of the superparamagnetic magnetic relaxation by local frustration in the mobility of magnetic moments caused by the local distribution of fields.³⁹

The presence of dipolar interactions clarifies the partially blocked state observed for the ZFC-FC curves and hysteresis loop at 310 K, and justifies as well the general decrease in magnetization. Furthermore, the presence of a small superficial organic layer (whose contribution could not be easily extrapolated in the mass calculation) also determines a general decrease of the magnetization values and at the same

Salafranca et al.⁴⁰ observed that variations in surface spin anisotropy of nanoparticles can be attributed to interactions occurring between the surface of the magnetic nanoparticle and the organic capping layer. The organics induce a bulk-like state for the superficial Fe sites, which results in an increase of the magnetisation at the surface of the particle. Thus, local changes in the density and thickness of the organic layer covering each nanoparticle influence the overall magnetic characteristics of the clusters. In particular, the higher density of magnetic particles implies a reduced organic coating around the individual nanoparticles within the iron oxide clusters. This increases spin disorder and finally, the spin frustration results in a reduced saturation magnetisation.²⁵

Magnetic resonance image contrast agents

Spatial and temporal resolution in MRI solely depends on the relaxation of net magnetisation of protons under static magnetic field. Contrast agents such as superparamagnetic iron oxide nanoparticles are able to accelerate the relaxation rate and thus provide a higher contrast image. Ideal T_2 weighted (negative) image contrast agents show low r_1 and high r_2/r_1 ratio. In literature there are several reports on the influence of nanoparticle size, shape and clustering on r_2 relaxivity.⁴¹⁻⁴³ Here, relaxivities of doped clusters are estimated by the slope of the linear fit of the curve obtained when plotting the relaxation time of proton as a function of both Fe and Mn concentration (see equation 2 at the materials and methods section) measured at different static magnetic field (0.5 T, 1 T and 1.5 T) and radio frequencies (20, 40 and 60 MHz).

Figure 6, shows that both r_1 and r_2 relaxivities are decreased with an increase in magnetic field and frequency, a typical behavior for ferri or ferromagnetic nanoparticles^{44,45}. The rate of relaxation of protons in the vicinity of magnetic nanoparticles is highly depended on the dipolar interactions between the spins of proton and spins of the contrast agent. On the other hand, it is well documented that the smaller the hydrodynamic size of the particles (R_H) and the higher the magnetic moments results in higher r_2 than r_1 relaxivity values. This is due to strong spin-spin interactions. In our experiments, the R_H of doped Mn-doped iron oxide clusters was about 54 nm, and resulted in a high r_2 relaxivity value of $571 \text{ mM}^{-1}\text{s}^{-1}$ at 0.5 T magnetic field and 20 MHz frequency. As the Mn-doped clusters exhibit ferrimagnetic behavior, r_2 decreases with further increase in magnetic field. These results are in agreement with previously reported values on analogue types of magnetic clusters⁴⁶. Also, the estimated r_1 values of Mn-doped iron oxide clusters were found to be 27 to $7 \text{ mM}^{-1}\text{s}^{-1}$ with increasing magnetic field and frequency. The numerical r_1 , r_2 and r_2/r_1 values of clusters are summarized in the Supporting Information-Table S2. Our observations that r_2/r_1 values increase from 20 to 65 with increasing magnetic field suggests that the doped CNCs are excellent candidates as a T_2 -weighted contrast agent.

Magnetic hyperthermia

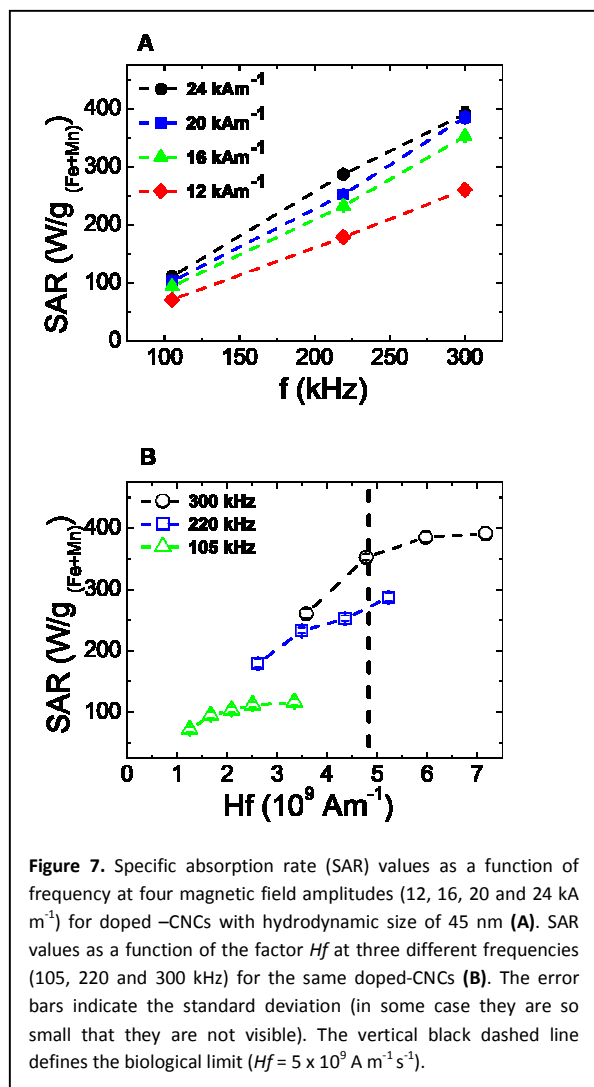


Figure 7. Specific absorption rate (SAR) values as a function of frequency at four magnetic field amplitudes (12, 16, 20 and 24 kA m^{-1}) for doped -CNCs with hydrodynamic size of 45 nm (A). SAR values as a function of the factor Hf at three different frequencies (105, 220 and 300 kHz) for the same doped-CNCs (B). The error bars indicate the standard deviation (in some case they are so small that they are not visible). The vertical black dashed line defines the biological limit ($Hf = 5 \times 10^9 \text{ A m}^{-1} \text{ s}^{-1}$).

time plays a physical role in the variations observed between the saturation magnetization values of clusters and individual nanoparticles.

The calorimetric measurement to quantify the heating performance of the Mn doped iron oxide clusters was done by exposing the aqueous sample to an alternating magnetic field (AMF) at different frequencies (105-220 and 300 kHz) and amplitudes (from 12 to 32 kA m⁻¹) and recording the variation of temperature over time. The specific absorption rate (SAR) ($W_{\text{Fe+Mn}}^{-1}$) is calculated by measuring the initial slope of the temperature vs. time curve (within the first milliseconds). The measurements are normalized to the concentration of iron and manganese taking into account the water heat capacity. The Mn-doped iron oxide clusters showed SAR values that are much higher than those ones obtained for individual iron oxide nanoparticles and comparable to other nanoparticle cluster structures.^{17, 47}

As shown in the **Figure 7A** the SAR values of the Mn-doped iron oxide clusters increase by increasing the frequency of the applied magnetic field following a linear trend in agreement with the linear response theory describing superparamagnetic nanoparticles.^{23, 48} An enhancement of the heating performance is also recorded keeping constant the frequency and increasing the field amplitude of the AMF (see Supporting Information Figure S4). However, this latest trend is not quadratic with the field amplitude as expected for isolated superparamagnetic NPs and in alignment to the linear response theory. Such intermediate behaviour might be due to the conformation of our clusters that is a secondary assembling of smaller superparamagnetic NPs resulting in a final ferromagnetic clusters. Indeed the highest SAR value ($390 \pm 10 W_{\text{Fe+Mn}}^{-1}$) was obtained for the strongest applied magnetic field (300 kHz and 32 kA m⁻¹). It is also important to note here that the high SAR values up to 350 W/g are recorded at field and frequency that are considered safe for patients, which means that significant high SAR values are reached at the values of the frequency and the magnetic field amplitude (Hf) that is smaller than $5 \times 10^9 \text{ A m}^{-1} \text{ s}^{-1}$.⁴⁹ As shown in **Figure 7B** (and **Figure S4B** in the Supporting Information), the Mn-doped clusters present very good SAR values especially below the safety threshold. In particular it is worth to note that in the safety region the Mn-doped clusters show much higher SAR values than those ones reported in literature for single manganese ferrite nanoparticles with various amounts of manganese.⁵⁰ While it would have been interesting to correlate these observations to the variation of Mn doping in CNCs as well as to undoped iron oxide clusters, the presence of Mn influences the morphological characteristics of the CNCs, making the comparison challenging. However, in our studies, iron oxide clusters with relevant morphological features to Mn-doped iron oxide clusters showed a significantly lower SAR across the range of field frequencies and amplitudes (see supporting information-Section 6). Furthermore, our Mn-doped iron oxide clusters cannot be directly compared to Mn-doped iron oxide nanoparticles^{51, 52} as their properties are directly correlated to the existence of their secondary nanoparticle structure.

In conclusion, we demonstrated a simple and robust method for the synthesis of highly concentrated Mn-doped iron oxide nanoparticle clusters in water. The clusters possess intrinsic

magnetic properties, which make them strong candidates for applications as contrast agents in MRI and as well as heat mediators in magnetic hyperthermia. The current study stimulates new ideas for the fabrication and application of three dimensional doped nanoparticle clusters in biomedicine with the ultimate aim to be the utilization of their enhanced magnetic properties as opposed to the current use of single nanoparticles.

Experimental Section

Materials: Diethylene glycol (DEG), 99.5%, was purchased from Fisher Scientific. Sodium Hydroxide (NaOH), anhydrous, Iron (III) chloride anhydrous, Manganese (II) chloride anhydrous, and polyacrylic acid (PAA) 1800 g/mol, were obtained from Sigma Aldrich.

Synthesis of Mn-doped iron oxide clusters: The clusters were prepared by modification of a chemical protocol for the formation of iron oxide clusters.²¹ In detail, sodium hydroxide (50 mmol) was dissolved in diethylene glycol (20 ml), under nitrogen. Then, the solution was refluxed to 120 °C for 1 hour, cooled down at 70 °C and it was retained for further use (stock solution). At a separate flask, iron chloride (III) (0.68 mmol), manganese (II) chloride (0.12 mmol) and polyacrylic acid (8 mmol) were dissolved in DEG (34 ml) and heated to 220 °C, under N₂ flow. Then, 3.4 ml of the NaOH /DEG stock solution were rapidly injected in the salt mixture. Few minutes after injection, the solution turned to black indicating the nucleation and growth of individual nanoparticles and consequently clusters. After 1 hour the reaction was quenched with ethanol and the solution was cooled to room temperature. The resulting product was purified by centrifugation at 6500 rpm for 15 min. Two additional purification steps were performed washing with a mixture of milliQ water and ethanol. Finally, the clusters were subjected to magnetic separation for 24 hours and redispersed in water.

Characterization of Mn-doped iron oxide CNCs: The morphology of the clusters was characterized by Transmission Electron Microscopy (TEM) using a Hitachi H-7000 microscope equipped with a W thermionic electron source operating at 125 kV. High Resolution Transmission Electron Microscopy (HRTEM) analysis was performed with a JEOL JEM-2200FS microscope equipped with a field emission gun working at an accelerating voltage of 200 kV, a CEOS spherical aberration corrector of the objective lens, which enables a spatial resolution of 0.9 Å, and an in column Omega filter. Chemical composition by Energy Dispersive X-ray Spectroscopy (EDS) was performed using a Bruker Quantax 400 system with a 60 mm² XFlash 6T silicon drift detector (SDD) according to the Cliff-Lorimer method. Samples for TEM analysis were prepared by depositing a drop of diluted nanocrystals solution onto 200 mesh a carbon-coated copper grid and then allowing the solvent to evaporate at room temperature.

Powder X-Ray Diffraction (XRD) measurements were carried out using a Panalytical Empyrean diffractometer equipped with a X'Celerator linear detector, using Cu K α radiation operating at 40 kV/40 mA and a monochromator on the diffracted beam. The scans were collected under sample spinning operating in θ - 2θ Bragg-

Brentano geometry within the range of 10°–90° (2θ) using a step size of 0.05 sec per step. Samples for XRD measurements were prepared by depositing some drops of concentrated colloidal dispersion in solution on a low background Si sample holder and then allowing the solvent to evaporate at room temperature. Phase identification was performed according to the Powder Diffraction File Database PDF-2 (International Centre for Diffraction Data 2007) and the determination of the mean crystallite diameter was estimated on the more intense peak using the Scherrer's equation.

Dynamic light measurements on magnetic clusters dispersed in water were performed on a Zetasizer Nano ZSP (Malvern Instrument) equipped with a 4 mW He-Ne laser operating at 633 nm. The measurements were conducted with disposable cuvettes (DTS0012) at 25°C. The data analysis was performed with 173° backscatter (NIBS default) as angle of detection. The measurement duration was set automatic and the measurements have been repeated three times. To obtain optically clear samples, 3 μl of sample were diluted in 1 ml of milliQ water.

Inductively coupled plasma-atomic emission spectrometry (ICP-AES Varian Liberty 200) was used to determine the Fe and Mn metal concentration in the samples. Sample preparation was achieved by acid desegregation (HCl/HNO₃, 3:1 volume ratio) of the nanoparticles at 90°C under reflux followed by partial solvent evaporation and dilution in water.

Static Magnetic Properties of Mn-doped CNCs: Magnetic characterization was performed on a Quantum Design MPMS SQUID magnetometer, equipped with a superconducting magnet producing fields up to 70 kOe. Zero-field-cooled (ZFC) and field-cooled (FC) magnetisations were collected in the range of temperatures 5–400 K. ZFC curves were measured by cooling samples in a zero magnetic field and by subsequent increase of the temperature under an applied field of 25 Oe. FC curves were recorded by cooling the samples while maintaining the same applied field of 25 Oe. Hysteresis loops were recorded up to ±20 kOe at 5.0 K and at 310.0 K. All the samples for SQUID analysis were prepared by dropping the colloidal dispersion of clusters onto a dielectric cotton substrate with a given mass and allowing for drying at ambient conditions, in order to minimize magnetic interactions among clusters. The data was normalized by the mass of the sample corrected for the contribution of the dielectric cotton.

Magnetic hyperthermia: All the measurements were carried out in a commercially available DM100 Series (nanoScale Biomagnetics Corp.) set up. To evaluate the SAR of the Mn-doped clusters in water, the sample (300 μl, 3.7 g/l of Fe and Mn) was introduced into a sample holder and exposed to an AC magnetic field at three different frequencies (105–220 and 300 kHz) under magnetic field amplitudes ranging from 12 to 32 kAm⁻¹. A fluoro-optic thermometer fiber probe (Luxtron Corp., CA) was used to probe the temperature versus time after switching on the alternating magnetic field (see supporting information -figure S5).

All the reported SAR values and error bars were calculated from the mean and standard deviation of at least three experimental measurements. SAR values were calculated according to the following equation:

$$SAR \left(\frac{W}{g} \right) = \frac{C}{m} \cdot \frac{dT}{dt} \quad \text{eq. (1)}$$

where C is the specific heat capacity of the solvent ($C_{\text{water}} = 4185 \text{ J L}^{-1} \text{ K}^{-1}$) and m is the concentration (g/l of Fe and Mn) of magnetic material in solution. Note that the final values are reported as ($W/g_{\text{Fe+Mn}}$). The measurements were carried out in non-adiabatic conditions, thus the slope of the curve dT/dt was measured by taking into account only the first few seconds of the curve (see supporting information Figure S5).

¹H Relaxivity measurements: Water solutions of Mn doped iron oxide clusters containing different Mn and Fe concentration ranging from 0.0005 to 1.1 mM were prepared. The longitudinal (T_1) and transverse (T_2) relaxation times were measured at 40 °C using a Minispec spectrometer (Bruker, Germany) mq 20 (0.5 T), mq 40 (1 T) and mq 60 (1.5 T). The T_1 relaxation profile was obtained using an inversion-recovery sequence, with 20 data points and 4 acquisitions for each measurement. T_2 relaxation time was measured using a Carr-Purcell Meiboom Gill (CPMG) spin-echo pulse sequence with 200 data points with inter echo time of 0.5 ms. The relaxivities r_i ($i = 1, 2$) were determined by the following equation:

$$\frac{1}{T_i} = \frac{1}{T_{i(\text{H}_2\text{O})}} + r_i C_{\text{Mn+Fe}} \quad (i = 1, 2) \quad \text{eq. (2)}$$

where C_{Fe} is the concentration of Fe and Mn ions. The values are reproducible within 5% deviation.

Acknowledgements

The University of Southampton is gratefully acknowledged for partial financial support of this project. A.G.K. would like to thank the EU COST action MP1202 for networking opportunities. MFC thanks the Fondazione Banco di Sardegna. TP acknowledges funding from the Italian AIRC project (contract no. 14527) and the Cariplo foundation (Contract No.20130865).

References

1. V. Schaller, G. Wahnström, A. Sanz-Velasco, S. Gustafsson, E. Olsson, P. Enoksson and C. Johansson, *Physical Review B*, 2009, **80**, 092406.
2. G. Chen, I. Roy, C. Yang and P. N. Prasad, *Chem. Rev.*, 2016, **116**, 2826–2885.
3. X. J. Loh, T.-C. Lee, Q. Dou and G. R. Deen, *Biomaterials Science*, 2016, **4**, 70–86.
4. D. Bartczak, O. L. Muskens, S. Nitti, T. M. Millar and A. G. Kanaras, *Biomaterials Science*, 2015, **3**, 733–741.
5. D. Ling, M. J. Hackett and T. Hyeon, *Nano Today*, 2014, **9**, 457–477.
6. R. Fernandes, N. R. Smyth, O. L. Muskens, S. Nitti, A. Heuer-Jungemann, M. R. Ardern-Jones and A. G. Kanaras, *Small*, 2015, **11**, 713–721.

- 7 7. B. Pelaz, P. del Pino, P. Maffre, R. Hartmann, M. Gallego, S. Rivera-Fernández, J. M. de la Fuente, G. U. Nienhaus and W. J. Parak, *ACS Nano*, 2015, **9**, 6996-7008.
- 8 8. M. Tebbe, C. Kuttner, M. Männel, A. Fery and M. Chanana, *ACS Applied Materials & Interfaces*, 2015, **7**, 5984-5991.
- 9 9. R. Fernandez-Montesinos, P. M. Castillo, R. Klippstein, E. Gonzalez-Rey, J. A. Mejias, A. P. Zaderenko and D. Pozo, *Nanomedicine*, 2009, **4**, 919-930.
- 10 10. M. Loumagne, J. R. G. Navarro, S. Parola, M. H. V. Werts and A. Debarre, *Nanoscale*, 2015, **7**, 9013-9024.
- 11 11. D. Ling, N. Lee and T. Hyeon, *Acc. Chem. Res.*, 2015, **48**, 1276-1285.
- 12 12. A. Heuer-Jungemann, P. K. Harimech, T. Brown and A. G. Kanaras, *Nanoscale*, 2013, **5**, 9503-9510.
- 13 13. A. Y. Rwei, W. Wang and D. S. Kohane, *Nano Today*, 2015, **10**, 451-467.
- 14 14. C. Blanco-Andujar, D. Ortega, P. Southern, S. A. Nesbitt, N. T. K. Thanh and Q. A. Pankhurst, *Nanomedicine*, 2015, **11**, 121-136.
- 15 15. C. Li, R. Ruan, M. Yang, F. Pan, G. Gao, S. Qu, Y.-L. Shen, Y.-L. Dang, K. Wang, W.-L. Jin and D.-Y. Cui, *Cancer Biology Medicine*, 2015, **12**, 163-174.
- 16 16. H. Kakwere, M. P. Leal, M. E. Materia, A. Curcio, P. Guardia, D. Niculaes, R. Marotta, A. Falqui and T. Pellegrino, *ACS Applied Materials & Interfaces*, 2015, **7**, 10132-10145.
- 17 17. R. Di Corato, A. Espinosa, L. Lartigue, M. Tharaud, S. Chat, T. Pellegrino, C. Ménager, F. Gazeau and C. Wilhelm, *Biomaterials*, 2014, **35**, 6400.
- 18 18. X. Meng, H. C. Seton, L. T. Lu, I. A. Prior, N. T. K. Thanh and B. Song, *Nanoscale*, 2011, **3**, 977-984.
- 19 19. M. F. Casula, P. Floris, C. Innocenti, A. Lascialfari, M. Marinone, M. Corti, R. A. Sperling, W. J. Parak and C. Sangregorio, *Chemistry of Materials*, 2010, **22**, 1739-1748.
- 20 20. Y.-X. J. Wang, *Quantitative Imaging in Medicine and Surgery*, 2011, **1**, 35-40.
- 21 21. J. Ge, Y. Hu and Y. Yin, *Angew. Chem. Int. Ed.*, 2007, **46**, 7428.
- 22 22. P. Hugounenq, M. Levy, D. Alloeyau, L. Lartigue, E. Dubois, V. Cabuil, C. Ricolleau, S. Roux, C. Wilhelm, F. Gazeau and R. Bazzi, *The Journal of Physical Chemistry C*, 2012, **116**, 15702-15712.
- 23 23. P. Guardia, R. Di Corato, L. Lartigue, C. Wilhelm, A. Espinosa, M. Garcia-Hernandez, F. Gazeau, L. Manna and T. Pellegrino, *ACS Nano*, 2012, **4**, 3080.
- 24 24. A. Kostopoulou and A. Lappas, *Nanotechnology Reviews*, 2015, **4**, 595-624.
- 25 25. A. Kostopoulou, K. Brintakis, M. Vasilakaki, K. N. Trohidou, A. P. Douvalis, A. Lascialfari, L. Manna and A. Lappas, *Nanoscale*, 2014, **6**, 3764-3776.
- 26 26. A. Kostopoulou, S. K. P. Velu, K. Thangavel, F. Orsini, K. Brintakis, S. Psycharakis, A. Ranella, L. Bordonali, A. Lappas and A. Lascialfari, *Dalton Transactions*, 2014, **43**, 8395-8404.
- 27 27. D. Sakellari, K. Brintakis, A. Kostopoulou, E. Myrovali, K. Simeonidis, A. Lappas and M. Angelakeris, *Materials Science and Engineering: C*, 2016, **58**, 187-193.
- 28 28. Y. S. Choi, H. Young Yoon, J. Sung Lee, J. Hua Wu and Y. Keun Kim, *Journal Of Applied Physics*, 2014, **115**, 17B517.
- 29 29. S. Xuan, F. Wang, Y.-X. J. Wang, J. C. Yu and K. C.-F. Leung, *Journal of Materials Chemistry*, 2010, **20**, 5086-5094.
- 30 30. J. Ge, Y. Hu, T. Zhang, T. Huynh and Y. Yin, *Langmuir*, 2008, **24**, 3671-3680.
- 31 31. H. Zhu, S. Zhang, Y.-X. Huang, L. Wu and S. Sun, *Nano Letters*, 2013, **13**, 2947-2951.
- 32 32. A. Taufiq, Sunaryono, E. G. Rachman Putra, A. Okazawa, I. Watanabe, N. Kojima, S. Pratapa and Darminto, *Journal of Superconductivity and Novel Magnetism*, 2015, **28**, 2855-2863.
- 33 33. J. Giri, P. Pradhan, V. Somani, H. Chelawat, S. Chhatre, R. Banerjee and D. Bahadur, *Journal of Magnetism and Magnetic Materials*, 2007, **320**, 724.
- 34 34. D. Peddis, C. Cannas, A. Musinu, A. Ardu, F. Orrù, D. Fiorani, S. Laureti, D. Rinaldi, G. Muscas, G. Concas and G. Piccaluga, *Chemistry of Materials*, 2013, **25**, 2005-2013.
- 35 35. G. F. Goya, T. S. Berquó, F. C. Fonseca and M. P. Morales, *Journal Of Applied Physics*, 2003, **94**, 3520-3528.
- 36 36. A. Kostopoulou, I. Tsiaoussis and A. Lappas, *Photonics and Nanostructures - Fundamentals and Applications*, 2011, **9**, 201-206.
- 37 37. J. Giri, P. Pradhan, V. Somani, H. Chelawat, S. Chhatre, R. Banerjee and D. Bahadur, *Journal of Magnetism and Magnetic Materials*, 2008, **320**, 724-730.
- 38 38. P. V. Melenev, V. V. Rusakov and Y. L. Raikher, *Technical Physics Letters*, 2008, **34**, 248-250.
- 39 39. S. Dutz, J. H. Clement, D. Eberbeck, T. Gelbrich, R. Hergt, R. Müller, J. Wotschadlo and M. Zeisberger, *Journal of Magnetism and Magnetic Materials*, 2009, **321**, 1501-1504.
- 40 40. J. Salafranca, J. Gazquez, N. Pérez, A. Labarta, S. T. Pantelides, S. J. Pennycook, X. Batlle and M. Varela, *Nano Letters*, 2012, **12**, 2499-2503.
- 41 41. M. E. Materia, P. Guardia, A. Sathya, M. Pernia Leal, R. Marotta, R. Di Corato and T. Pellegrino, *Langmuir*, 2015, **31**, 808-816.
- 42 42. F. Xu, C. Cheng, D.-X. Chen and H. Gu, *ChemPhysChem*, 2012, **13**, 336-341.
- 43 43. M. Levy, A. Quarta, A. Espinosa, A. Figuerola, C. Wilhelm, M. García-Hernández, A. Genovese, A. Falqui, D. Alloeyau, R. Buonsanti, P. D. Cozzoli, M. A. García, F. Gazeau and T. Pellegrino, *Chemistry of Materials*, 2011, **23**, 4170-4180.
- 44 44. H. B. Na, I. C. Song and T. Hyeon, *Advanced Materials*, 2009, **21**, 2133-2148.
- 45 45. E. D. Smolensky, H.-Y. E. Park, Y. Zhou, G. A. Rolla, M. Marjańska, M. Botta and V. C. Pierre, *Journal of*

- materials chemistry. B, Materials for biology and medicine*, 2013, **1**, 2818-2828.
- 46 46. T.-J. Yoon, H. Lee, H. Shao, S. A. Hilderbrand and R. Weissleder, *Advanced Materials*, 2011, **23**, 4793-4797.
- 47 47. J. P. Fortin, C. Wilhelm, J. Servais, C. Ménager, J. C. Bacri and F. Gazeau, *Journal of the American Chemical Society*, 2007, **129**, 2628-2635.
- 48 48. R. E. Rosensweig, *Journal of Magnetism and Magnetic Materials*, 2002, **252**, 370.
- 49 49. R. Hergt and S. Dutz, *Journal of Magnetism and Magnetic Materials*, 2007, **311**, 187-192.
- 50 50. A. Doaga, A. M. Cojocariu, W. Amin, F. Heib, P. Bender, R. Hempelmann and O. F. Caltun, *Materials Chemistry and Physics*, 2013, **143**, 305.
- 51 51. E. Mazarío, J. Sánchez-Marcos, N. Menéndez, M. Cañete, A. Mayoral, S. Rivera-Fernández, J. M. de la Fuente and P. Herrasti, *The Journal of Physical Chemistry C*, 2015, **119**, 6828-6834.
- 52 52. A. Makridis, K. Topouridou, M. Tziomaki, D. Sakellari, K. Simeonidis, M. Angelakeris, M. P. Yavropoulou, J. G. Yovos and O. Kalogirou, *Journal of Materials Chemistry B*, 2014, **2**, 8390-8398.

53